Chapter 11
Influence of Low-Level Jets and Gravity Waves on Turbulent Fluxes

Andrei Serafimovich, Jörg Hübner, Monique Y. Leclerc, Henrique F. Duarte, and Thomas Foken

11.1   Introduction

The vertical wind distribution within the atmospheric boundary layer is an important weather phenomenon and has a significant impact on ecological processes. Numerous experiments carried out at the FLUXNET (Baldocchi et al. 2001) station DE-Bay near the Weidenbrunnen in the Fichtelgebirge observe a secondary wind

A. Serafimovich (✉)
Helmholtz Centre Potsdam, GFZ German Research Centre for Geosciences, Telegrafenberg, 14473 Potsdam, Germany
e-mail: andrei.serafimovich@gfz-potsdam.de

J. Hübner
Uhl Windkraft Projektierung GmbH & Co. KG, Max-Eyth-Str. 40, 73479 Ellwangen, Germany

M.Y. Leclerc
Atmospheric Biogeosciences Lab, The University of Georgia, Griffin, GA 30223, USA

H.F. Duarte
Department of Atmospheric Sciences, College of Mines and Earth Sciences, University of Utah, Salt Lake City, UT 84112-0102, USA

T. Foken
Am Herrgottsbaum 28, 96120 Bischberg, Germany

Bayreuth Center of Ecology and Environmental Research, University of Bayreuth, Bayreuth, Germany

A. Serafimovich, J. Hübner, T. Foken: Affiliation during the work at the Waldstein sites: Department of Micrometeorology, University of Bayreuth, Bayreuth, Germany

H.F. Duarte: Affiliation during the work at the Waldstein sites: Atmospheric Biogeosciences Lab, The University of Georgia, Griffin, GA 30223, USA

maximum around the first decameters above the ground (Thomas et al. 2006; Thomas and Foken 2007b). It is well known that in the case of stable stratification of the atmospheric boundary layer, the topography has a strong influence on the wind field up to several hundred meters above the ground. Therefore, the nocturnal phenomena in the atmospheric boundary layer such as the low-level jet (LLJ) responsible for shear processes and resulting in high turbulence near the ground surface (Banta et al. 2002; Karipot et al. 2006) should not be neglected in the analysis of wind profiles. It is important to investigate the occurrence of LLJs and to examine the relationships between the jet properties, generated turbulence, and the related transport of energy and matter.

Wind shear is one of the main sources of gravity waves. Gravity waves are an essential part of the dynamics of the atmosphere over a wide band of meteorological scales. Their importance as a source of energy and momentum transport is widely accepted. Due to their wide range of wavelengths and periods, phase and group speeds, the propagation of gravity waves affects a wide range of atmospheric phenomena on large synoptic to micrometeorological scales. The energy and momentum transported by gravity waves is transferred to the mean flow (Nappo 2012) or dissipated in the form of turbulence (Einaudi and Finnigan 1993; Smedman et al. 1995), enhancing turbulent transport when the wave becomes unstable and breaks. Most gravity wave studies are carried out using the linear wave theory (Gossard and Hooke 1975; Lindzen and Tung 1976) providing, under linearization of the primitive set of equations for an inviscid, non-rotating fluid, relationships between wind components, temperature, pressure, and air density.

In recent studies, investigation of gravity waves and their effects on atmospheric phenomena is carried out on different scales. For example, large scale gravity waves having horizontal periods on the order of hundreds and thousands of kilometers are studied using synoptic or mesoscale approaches. The large scale gravity waves interact with breaking Rossby waves (Zülicke and Peters 2006), clouds and precipitation (Koch and O'Handley 1997), damaging winds (Pecnick and Young 1984), and multiple layers of polar mesosphere summer echoes (Hoffmann et al. 2005). The small scale gravity waves have been studied from the micrometeorological point of view. These waves occur mostly in stably stratified atmospheric layers close to the surface during the nighttime in the nocturnal boundary layer or in the long-lived stable boundary layer in polar regions (King et al. 1987; Rees et al. 2001; Sun et al. 2003).

Another important phenomenon in the atmospheric boundary layer is that of coherent structures. Over the past few decades, coherent structures have become a key point of many studies in the turbulence research of flow dynamics in laboratory flows and the atmospheric boundary layer (Raupach and Thom 1981; Bergström and Högström 1989; Gao et al. 1989; Shaw et al. 1989; Paw U et al. 1992; Raupach et al. 1996; Brunet and Irvine 2000; Thomas and Foken 2007b). Coherent structures appear in measurements of wind, temperature, or scalar concentration

as approximate periodic ramps connected with the ejection-sweep cycles (Katul et al. 1997; Finnigan 2000; Foster et al. 2006) and contribute significantly to the turbulent transport above and within the canopy (Maitani and Shaw 1990; Katul et al. 1997; Thomas and Foken 2007a). As was shown by Raupach et al. (1996) and Finnigan (2000), in the simplest cases of planar homogeneous and stationary flows, the sources of coherent structures above plant canopies are Kelvin-Helmholtz instabilities observed in plane mixing layers. Brunet and Irvine (2000) then demonstrated that the mixing layer analogy applies in a variety of plant canopies for an expanded range of atmospheric stabilities.

The interactions between the mean flow, waves, and turbulence, and coherent structure generation in the presence of gravity waves are the key points of many recent studies. Einaudi and Finnigan (1993) investigated wave-turbulence coupling. Nappo et al. (2008) studied the influence on plume dispersion of an internal gravity wave following a pressure jump. The impact of wave breaking or Kelvin-Helmholtz shear instability on wave-induced turbulent diffusion was examined in the works of Sun et al. (2003) and Cheng et al. (2005). A number of studies reported simultaneous occurrence of gravity waves in the vicinity of the canopy (canopy waves) and ramps near the canopy top (Paw U et al. 1992; Lee et al. 1997), suggesting that canopy waves are produced by Kelvin-Helmholtz instabilities induced by the strong wind shear.

However, interactions between coherent structures and waves are still poorly understood, and a generalized theory regarding turbulent mixing and turbulent flux exchange in the presence of periodic atmospheric wave motions is missing. On the other hand, there is a relative lack of studies dealing with the local effects produced by gravity waves propagating along a specific measuring site. The main objective of this work is to study a gravity wave in conjunction with a strong wind shear event and to develop a comprehensive analysis of the wave characteristics using linear theory. The effects of the wave propagation close to the surface and their impact on coherent structures and turbulent exchange in the vicinity of a tall canopy will be examined.

11.2 Material and Methods

11.2.1 Experimental Setup

The results presented here were obtained in the frame of the EGER project (ExchanGE processes in mountainous Regions). This project is focused on the detailed investigation of interaction processes at different scales and their role in the budgets of energy and matter within the soil-vegetation-atmosphere system. The overview of the project can be found in Foken et al. (2012) and Chap. 1.

Data were obtained in the period of June–July 2008 and 2011 during the second and third intensive measuring campaigns (IOP 2 and IOP 3) of the project. The experiment was carried out at the FLUXNET site Waldstein-Weidenbrunnen (DE-Bay, 50°08′N, 11°52′E). The site is located at an altitude 775 m a.s.l. in the Fichtelgebirge Mountains in North-Eastern Bavaria, Germany. The coniferous canopy mainly consists of spruce trees with mean canopy height $h_c = 25$ m. A detailed description of the site is given in Gerstberger et al. (2004), and the reference data can be found in Staudt and Foken (2007) and Chap. 2.

The experimental design of the second intensive observation period IOP 2 almost repeats the design of the first campaign IOP 1. More details about instrumentation can be found in Serafimovich et al. (2011) and Appendix A. High-frequency measurements (20 Hz) of wind components (u, v, w), sound temperature T_s, density of carbon dioxide CO_2 and water vapor H_2O were performed. Six ultrasonic anemometers (USA-1 Metek GmbH, CSAT3 Campbell Scientific, Inc., Solent R2 Gill Instruments Ltd.) and six fast-response gas analyzers (LI-7000 and LI-7500, LI-COR Biosciences) were installed on the 36 m tall tower (Turbulence Tower, TT) at 0.09, 0.22, 0.52, 0.72, 0.92, 1.44 h_c levels, and an ultrasonic anemometer and a fast-response gas analyzer were installed at 1.28 h_c level on the second 32 m tall tower (Main Tower, MT) standing 60 m away from the above tower.

The atmospheric boundary layer was profiled with an acoustic and radioacoustic radar remote sensing system SODAR-RASS. The measurements were performed with a system consisting of a phase array Doppler SODAR DSDPA.90–64 with a 1290-MHz-RASS extension by Metek GmbH. The acoustic sounding system was located at a distance of approximately 250 m from the towers in a forest clearing. Two operating modes were used. Vertical wind speed and temperature were measured using the first mode for 25 min. The vertical range of measurements was from 20 to 200 m a.g.l. In the second mode the atmospheric boundary layer was profiled for a period of 5 min up to an observational level of 900 m, using a vertical resolution of 30 m. This gave a mean profile of the wind vector. A second SODAR (referred to as miniSODAR, Scintec AG) without a RASS extension was installed 500 m away and provided 5-min mean profiles up to 200 m a.g.l. These measurements were extended by the data from the 482 MHz windprofiler of the German Weather Service at Bayreuth (Northern Bavaria, Germany), located 22 km to the South–West of the Waldstein measuring site. The windprofiler measured vertical profiles of the horizontal wind vector and virtual temperature in the atmosphere. The technical data of the radar system are given in Lehmann et al. (2003). During the IOP 3 the miniSODAR system (Scintec AG) was installed at the forest edge 250 m to the south-east from the MT.

In addition, the measurements at MT provide meteorological data of wind, temperature, humidity, and radiative fluxes within and above the canopy.

11.2.2 Instruments: Principles of Operation

Radar Wind Profiler (RWP) and SODAR (SOund Detecting And Ranging) are active remote sensing systems for ground-based observations of wind in the atmosphere. Both systems can be extended by the Radio Acoustic Sounding System (RASS) to measure virtual temperature profiles.

11.2.2.1 Windprofiler/SODAR

The principles of measurements of atmospheric turbulence by means of either electromagnetic or acoustic waves do not differ fundamentally. RWP systems transmit electromagnetic waves with known frequencies in the VHF (30–300 MHz) and UHF (300–3000 MHz) ranges in the atmosphere. The corresponding wavelengths are on the order of 1.0–10.0 m in the VHF and 0.1–1.0 m in the UHF ranges (Clifford et al. 1994). These waves will be affected by atmospheric processes such as reflection, scattering, refraction, and absorption, and their properties such as propagation direction, phase, and signal strength will be changed. In this case, the RWP primarily uses the backscattering of electromagnetic waves due to natural fluctuations in the refractive index, which in the frequency band of the RWP is a function of temperature and water vapor pressure. The influence of the atmospheric pressure p is negligible (Sauvageot 1992).

The DBS method uses three to five beams emitted in series in different directions. One of the beams is always in the vertical direction and the other beams are tilted from the vertical at a predetermined angle α. Depending on the transmitted frequency, the frequency of backscattered echo will be shifted due to the Doppler effect, and this can be used for direct measurements of the radial wind speed v_r:

$$v_r = \frac{\Delta f \lambda}{2}, \tag{11.1}$$

where Δf is the Doppler shift between the transmitted and received frequency and the wavelength λ results from the ratio between the propagation speed c of the wave and transmission frequency f:

$$\lambda = \frac{c}{f}. \tag{11.2}$$

Successive measurements carried out under the assumption of homogeneous conditions in three non-coplanar directions in space allow the calculation of the 3D wind vector. However, the assumption of homogeneity is usually valid for averaging over long time periods. Varying of the beam direction is controlled by a phase-shifted signal generated by a phased array antenna composed of numerous transmitting elements and a phase shifter.

The three wind components u, v, and w can be obtained from the radial wind velocities v_{rx} calculated as follows (index x characterizes the different beam directions, 1 and 2 are tilted antennas, 3 is vertical antenna):

$$u(z) = \frac{v_{r1}(z) - v_{r3}(z)\cos\alpha}{\sin\alpha}, \tag{11.3}$$

$$v(z) = \frac{v_{r2}(z) - v_{r3}(z)\cos\alpha}{\sin\alpha}, \tag{11.4}$$

$$w(z) = v_{r3}(z). \tag{11.5}$$

The measuring principle of the SODAR system is very similar to the RWP. Instead of electromagnetic waves, acoustic waves with much lower transmission frequencies (1–4 kHz) are emitted. The corresponding wavelengths are in the order of 0.09 to 0.35 m (Clifford et al. 1994). While electromagnetic waves are propagated at light speed, the speed of acoustic waves is significantly lower: approximately $343\,\text{ms}^{-1}$ for air with normal humidity and a temperature of $20\,°C$. Due to this massive difference in the propagation velocity and the resulting longer detection time, acoustic waves provide better spatial resolution. However, due to the smaller wavelength and stronger attenuation in the atmosphere, the range of the acoustic waves is significantly lower.

11.2.2.2   RASS

The RASS principle is based on the measurement of temperature-dependent sound speed using backscattering of radio waves from an acoustic wave front. The RASS system consists of an acoustic wave and electromagnetic wave transmitters. The acoustic wave transmitted in the atmosphere modulates the refractive index. If the acoustic wavelength matches the Bragg wavelength of the radar (half of the radar wavelength), an enhanced backscattered echo will be observed. Due to the Doppler effect, the frequency of the backscattered echo will be shifted by the velocity of the acoustic wave front. The Bragg condition is fulfilled in different heights by different wavelengths of acoustic waves. Therefore, varying the frequency of the acoustic wave, detecting the heights of the enhanced backscattered signal, and using the known relationship between the speed of sound and the virtual temperature T_v, the profiles of T_v can be derived.

11.2.3 Data Calculation

To detect wave motions and coherent structures from observed time series, the spectral analysis using wavelet transform has been used. A detailed discussion about data preparation and wavelet analysis can be found in Thomas and Foken (2005). Here the main steps will be summarized.

Using a despiking test (Vickers and Mahrt 1997) with a window length 300 s and initial criteria of 6.5 standard deviations, outliers in 20 Hz high-frequency series were removed. Wind vector components were rotated sector-wise on a monthly basis according to planar fit rotation methods (Wilczak et al. 2001). To account for delays in sensor response and data recording, time series of scalar components were corrected for time lags. Comparing time series of carbon dioxide and water vapor concentrations s with vertical wind component w and finding the maximum of $\overline{w'(t)s'(t + \Delta t)}$, where the prime denotes the oscillation part of the signal and the overbar denotes time averaging, time lags were estimated.

Nowadays the wavelet technique has become a standard tool for the detection of wave motions and coherent structures in measurements. Due to the ability of the wavelet spectrum to be resolved in time and height, this technique gives additional information about wave structure and location. A more detailed review of the wavelet applications in geophysics can be found in Kumar and Foufoula-Georgiou (1997) or Torrence and Compo (1998). Wavelet transform is successfully applied to detect gravity waves in the atmosphere (Zink and Vincent 2001) and coherent structures in the vicinity of a tall canopy (Thomas and Foken 2005).

The wavelet transform itself denotes the correlation between measured function $f(t)$ observed at fixed location and the version of the mother wavelet, which is scaled with a factor a and translated by a dilation b:

$$T_p(a, b) = \frac{1}{a^p} \int_{-\infty}^{+\infty} f(t) \Psi\left(\frac{t - b}{a}\right) dt, \tag{11.6}$$

where $T_p(a, b)$ are the wavelet coefficients, a the dilation scale, b the translation parameter, p the normalization factor ($p = 1$ in our case), and Ψ the Morlet wavelet function. As in many other geophysical studies, the Morlet wavelet was used in this analysis due to a good localization in the frequency domain, with it exhibiting only one distinct peak (Pike 1994). The wavelet variance spectrum $W_p(a)$ is then determined by

$$W_p(a) = \int_{-\infty}^{+\infty} \left|T_p(a, b)\right|^2 db. \tag{11.7}$$

Both wavelet coefficients and wavelet variance spectrum give the information about predominant frequencies and wavelengths in the background wind flow.

To reduce computation time for the wavelet analysis, all time series were block averaged to a 2 Hz resolution. Finally, all time series were passed through a low-

pass wavelet filter to remove small-scale high-frequency turbulence. According to the spectral gap between high-frequency turbulence and low-frequency coherent structures, the critical event duration D_c was chosen to be 6.2 s, which is in close agreement with values used in other studies (Brunet and Collineau 1994; Chen and Hu 2003). To detect coherent structures, the time series $f(t)$ were zero-padded and a continuous wavelet transform (Grossmann and Morlet 1984; Kronland-Martinet et al. 1987) using the Morlet wavelet was performed (Eq. (11.6)). For the following estimation of coherent structures, the wavelet variance spectrum $W_p(a)$ (Eq. (11.7)) was determined. The characteristic duration of coherent structures for each 30 min time interval was obtained by the location of the maximum of the wavelet variance spectrum. Finally, according to Thomas and Foken (2007a), Reynolds-averaged flux and flux contribution of coherent structures were derived using a conditional sampling analysis and averaging method (Antonia 1981).

Following Thomas and Foken (2007a), the exchange regimes between air above the canopy, the canopy, and the trunk space were investigated. This method is based on the analysis of the portion of the sensible heat exchange by coherent structures between three levels: subcanopy level, canopy level, and air above the canopy. One can define the following exchange regimes:

- Wa – wave motion. There is no turbulence above the canopy, the linear gravity waves dominate in the flow.
- Dc – decoupled canopy. Turbulent motions are present above the canopy, but there is no coherent transport between the canopy and the atmosphere.
- Ds – decoupled subcanopy. The coherent exchange takes place only between the canopy and the atmosphere, the trunk space is decoupled.
- Cs – coupled by sweeps. The sweep phases of coherent structures are responsible for the exchange of energy and matter between atmosphere, canopy, and subcanopy. The role of ejection phases is insignificant.
- C – fully coupled canopy. The atmosphere, canopy, and the trunk space of the forest are fully coupled by coherent structures.

For more details see Chap. 6.

11.2.4 Meteorological Situation

As shown by the wind rose (Fig. 11.1), over the canopy at the Waldstein site prevail west and south-east winds with wind speeds on the order of 2–5 ms^{-1}. Such a west wind was observed during the daytime from 9:00 to 20:00 on 30 June, 2008 (Fig. 11.2). The wind speed increased to reach the maximum 4 ms^{-1} at noon and then fell to 1.2 ms^{-1}. At 20:00 the wind started to change its direction and increase in amplitude. This effect lasted for 4 h till 24:00. During this period the wind speed increased to 3.7 ms^{-1} with wind gusts up to 6.8 ms^{-1} and then decreased to 2.1 ms^{-1}, and the wind changed direction from west to south-east.
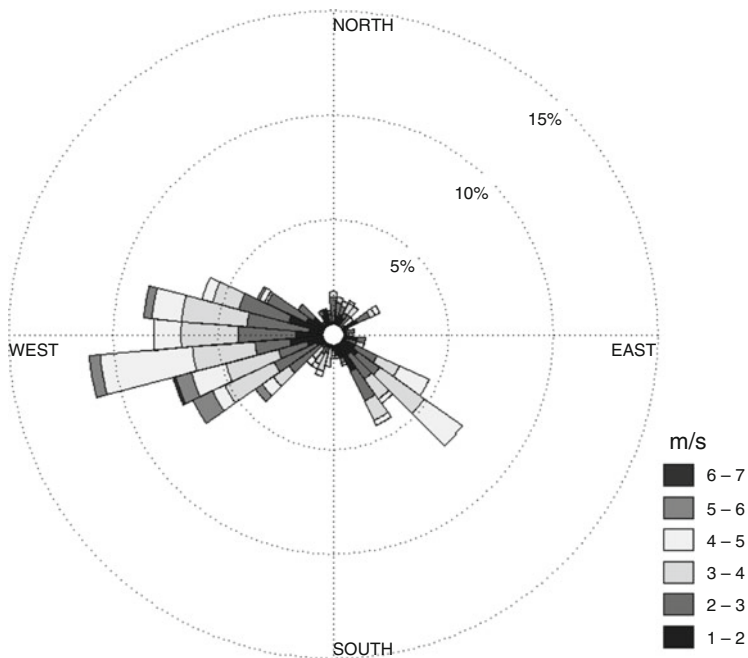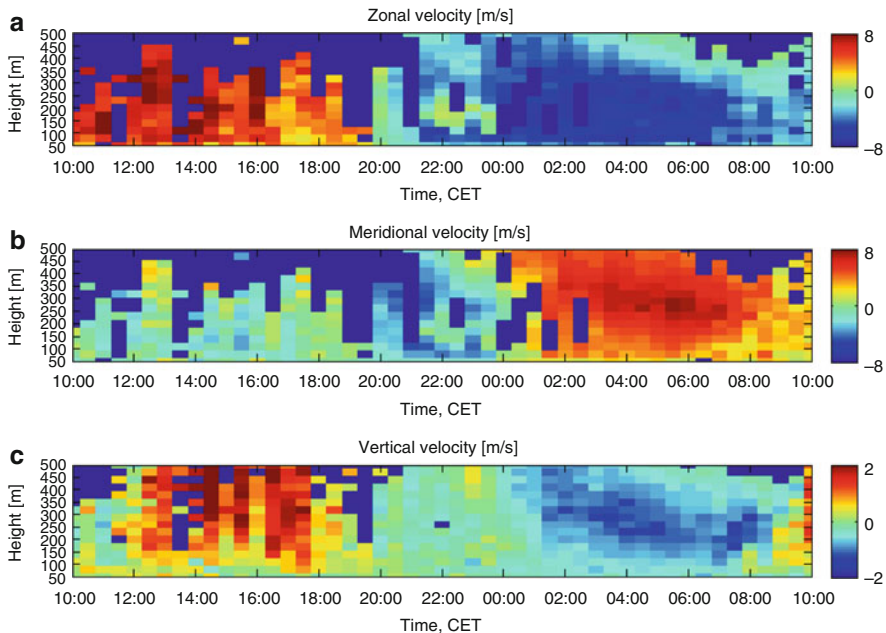
Fig. 11.1 Wind rose derived from the measurements at TT at 36 m height for the period June 17–July 02, 2008 during IOP 2
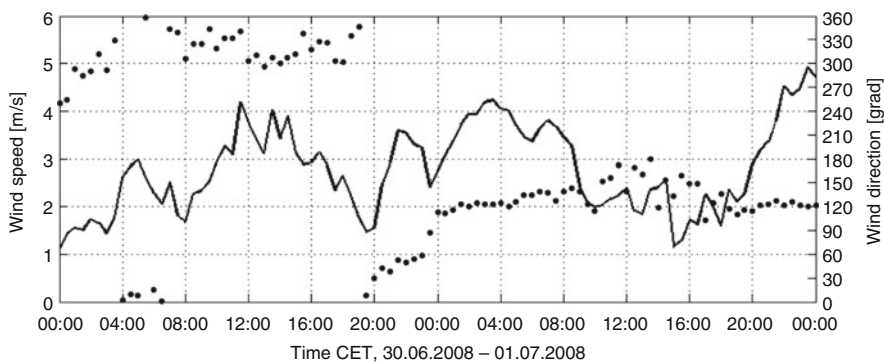
Fig. 11.2 Mean wind speed (*line*) and wind direction (*dots*) averaged for 30 min at MT at 32 m height for the period June 30–July 01, 2008 during IOP 2
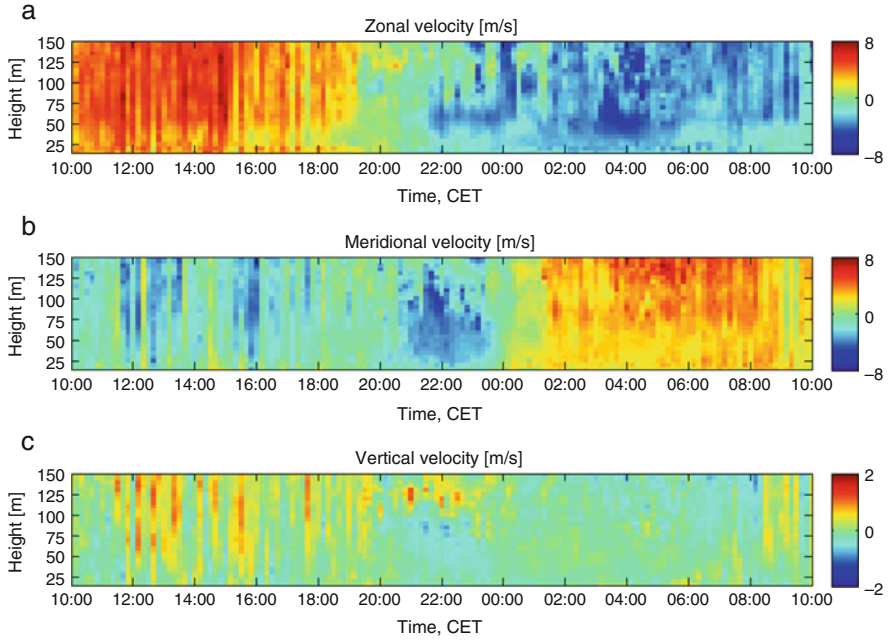
Fig. 11.3 Zonal (**a**), meridional (**b**), vertical (**c**) velocities measured with SODAR/RASS for the period 10:00 June 30–10:00 July 01, 2008 during IOP 2. Dark blue color corresponds to gaps

Figure 11.3 shows height-time cross-sections of the zonal, meridional, and vertical wind components observed by the SODAR/RASS system over Waldstein site. During the daytime on June 30 in the atmospheric boundary layer the meridional wind was weak, whereas a strong zonal wind component on the order of $8\,\mathrm{ms}^{-1}$ indicates a westerly wind. As mentioned above, the situation changes at 20:00 CET. The zonal wind component decreases until 01:00 CET and reaches $-8\,\mathrm{ms}^{-1}$, and the meridional wind component increases until 01:00 CET and reaches a clear maximum on the order of $8\,\mathrm{ms}^{-1}$ between 250 and 350 m at 05:00 CET. The vertical wind component is mostly positive during the daytime on June 30, then falls to small values around zero at 24:00 and reaches the negative maximum at 04:00 CET. The situation observed describes the evaluation of an LLJ with a strong shear effect.

Due to the effect of environmental noise, the SODAR/RASS data unfortunately contain a lot of gaps during the period of the wind rotation (dark blue area in Fig. 11.3). Therefore, for the following analysis the wind measurements observed with the miniSODAR system will be used. As shown in Fig. 11.4, smoothed zonal, meridional, and vertical winds derived from these data confirm a wind rotation effect and wind maxima detected by the SODAR/RASS system and described above.

Figure 11.5 shows the exchange regimes observed at the Waldstein site for the period June 30–July 2, 2008. The principle of the method is described in Thomas and Foken (2007a) and Chap. 6. When wind begins to rotate at 20:00 on June 30 the

Fig. 11.4 Zonal (**a**), meridional (**b**), vertical (**c**) velocities averaged for 10 min measured with miniSODAR for the period 10:00 June 30–10:00 July 01, 2008 during IOP 2
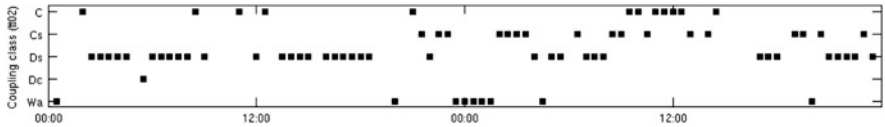
Fig. 11.5 Characterization of the turbulent exchange regimes for the period June 30–July 02, 2008 during IOP 2. Wa, Dc, Ds, Cs, C indicate wave motion, decoupled canopy, decoupled subcanopy, coupled subcanopy by sweeps, and fully coupled states

"fully coupled C" state changes to the "coupled by sweeps Cs" with the following "decoupled subcanopy Ds" state, and finally coming to the state "wave motion Wa" around midnight, suggesting that the atmospheric wave motion occurs above the measuring site.

As demonstrated by Baas and Driedonks (1985), Paw U et al. (1992), and Cava et al. (2004), waves are an important phenomena near the canopy level. In the following sections evidence of the wave motion above the Waldstein forest site and the impact of waves on the turbulent transport will be discussed.

11.3   Results and Discussion

11.3.1   Low-Level Jets

An LLJ is a strong wind whose maximum speed may be in the order of $10–20\,ms^{-1}$. This maximum can be found mostly at an altitude of $100–300\,m$ above ground (Stull 1988). Various criteria for the identification of LLJs can be found in the scientific literature. Bonner (1968) categorized LLJs based on speed and height occurrence of jets. The pragmatic definition of LLJ can be specified as follows: the LLJ exists if the observed maximum of the wind speed is $2\,ms^{-1}$ larger than the wind speed in the remaining overlying atmospheric boundary layer (Stull 1988). Other definitions of LLJ, based on physical aspects of the wind in the boundary layer, can be found in Blackadar (1957) and Holton (1967).

The LLJ at the Waldstein site usually originates from south-east and south-west (Fig. 11.6), coming along with negative vertical winds (downward), a well-coupled system and good mixing. Only during weakened LLJ events and/or the formation of gravity waves above the forest canopy is an accumulation of CO_2 within the trunk space observable.

An example of an LLJ observed from 30 June to 1 July 2008 is shown in Fig. 11.7. The wind velocity of the jet was found to be above $10\,ms^{-1}$ for about 6 h at a height of 300 m, temporally descending to 200 m. The wind direction of the LLJ was SE, while above the LLJ the wind direction moved from SE over S to W. In the LLJ the vertical wind was negative (downward).

In Fig. 11.8, vertical distributions of NO and O_3 concentrations are shown during the LLJ event shown in Fig. 11.7. Due to the increased shear, a better mixing was found during the period with the LLJ between 02:00 and 08:00, with a maximum at 04:00. The better mixing resulted in a reduction of concentrations accumulated near the surface (Fig. 11.8). In the early morning, at approximately 04:00, when
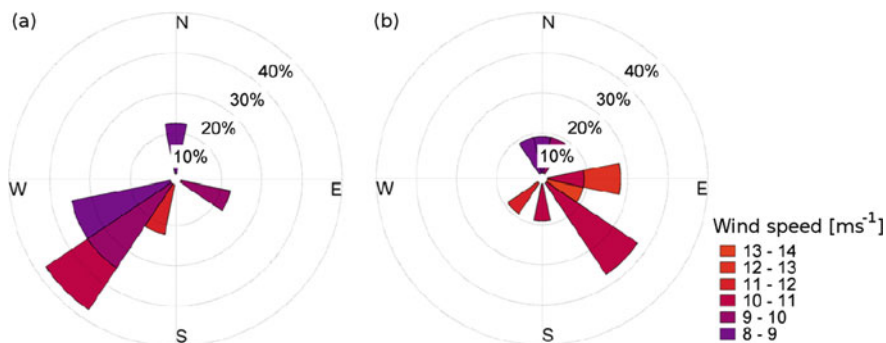

Fig. 11.6 Wind roses for all LLJ events (**a**) during the IOP 1 period ($n = 8$) and (**b**) during the IOP 2 period ($n = 11$). Maximum achieved wind speed and the wind direction measured at the same height are used
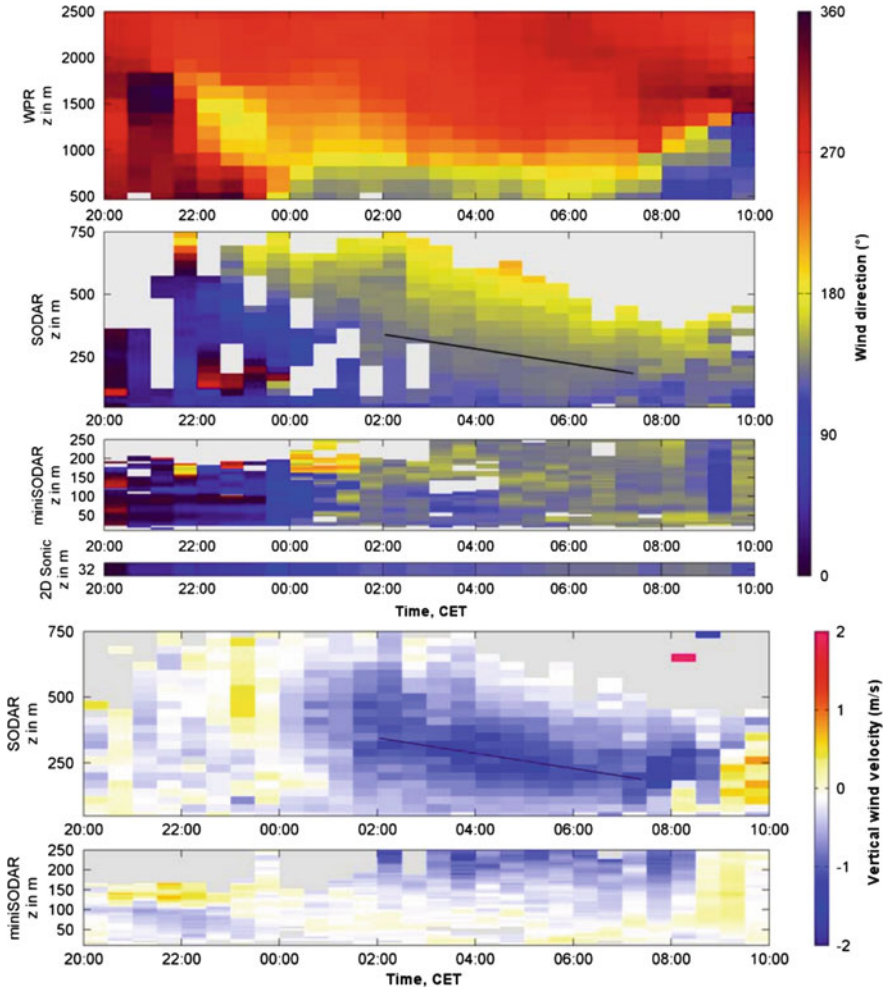
Fig. 11.7 Time-height profile from windprofiler, sodar, mini-sodar and sonic data of the wind direction (*above*), and vertical wind velocity (*below*) in the night from 30 June to 1 July 2008. The axis of the low-level jet is highlighted (Foken et al. 2012), published with kind permission, ©Authors 2012, CC Attribution 3.0 License, All rights permitted

the LLJ occupied lower heights, the atmosphere close to the surface is suddenly mixed resulting in high NO concentrations, probably representing an outflow of the upper Eger river valley during easterly winds. The most impressive is the inflow of fresh air with high O_3 concentrations between 22:00 and 24:00, connected with the occurrence of gravity waves.

During IOP 3 an LLJ event occurred in the night from 27 June 22:00 CET to 28 June 08:00 CET. These days were hot and dry (see Chap. 14), which facilitated the formation of LLJ events (Fig. 11.9). Maximum wind velocities up to $10\,\mathrm{ms}^{-1}$
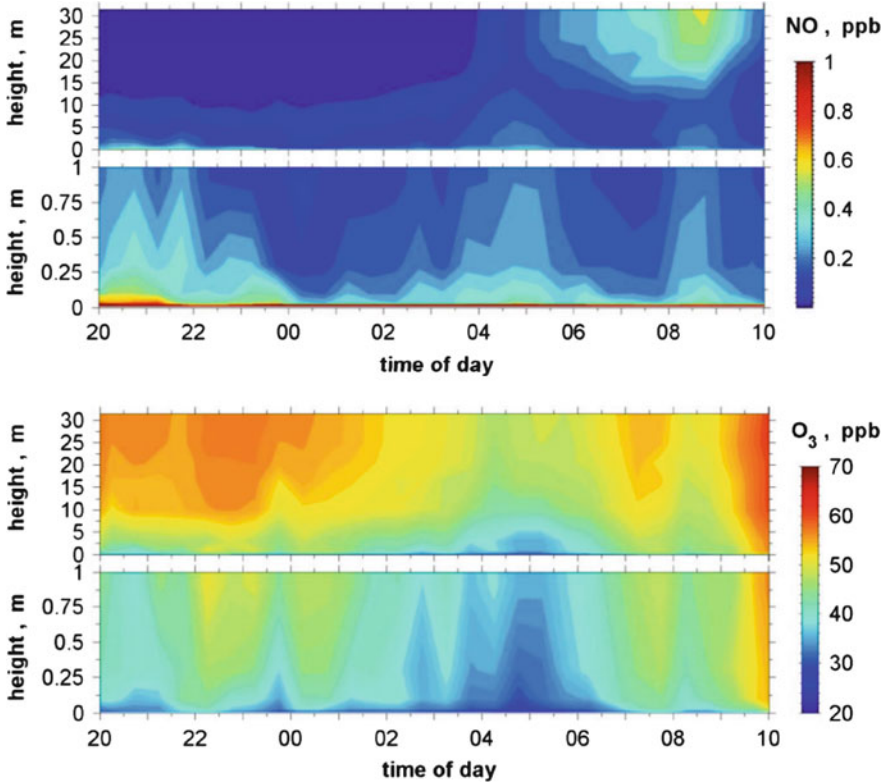
Fig. 11.8 Averaged vertical profiles in the night from 30 June to 1 July 2008 (CET time) for NO and O3 (Foken et al. 2012), published with kind permission, ©Authors 2012, CC Attribution 3.0 License, All rights permitted

occurred between the heights of 180–220 m from 22:00 to 00:30 CET. After 00:30 CET, a weakened LLJ event could be observed around the height of 100 m with wind velocities up to $7\,\mathrm{ms}^{-1}$. The vertical winds were negative (downward) over the total time of the LLJ, with a maximum of $-1\,\mathrm{ms}^{-1}$, and the typical south to south-easterly winds were prevailing. CO_2 fluxes were up to 7–$12\,\mu\,\mathrm{mol}\,\mathrm{m}^{-2}\,\mathrm{s}^{-1}$.

Figure 11.10 presents the horizontal profiles measured with the horizontal mobile measuring system (HMMS) during this LLJ event. The HMMS is described in Hübner et al. (2014) and Chap. 14. During 20:00–22:00 CET (northerly winds), there is a CO_2 concentration maximum (Fig. 11.10b) near the forest edge, which confirmed the assumption of changed turbulent structures caused by the forest edge. Also temperature (Fig. 11.10a) was lower near the edge. At the clearing the CO_2 concentration was equal to the atmospheric concentration of around 380 ppm. Between 22:00 and 00:30 CET, the conditions at the site changed significantly, and the LLJ with southerly winds and higher wind velocities prevailed. First the lower CO_2 concentration was blown into the forest and the horizontal profile was nearly
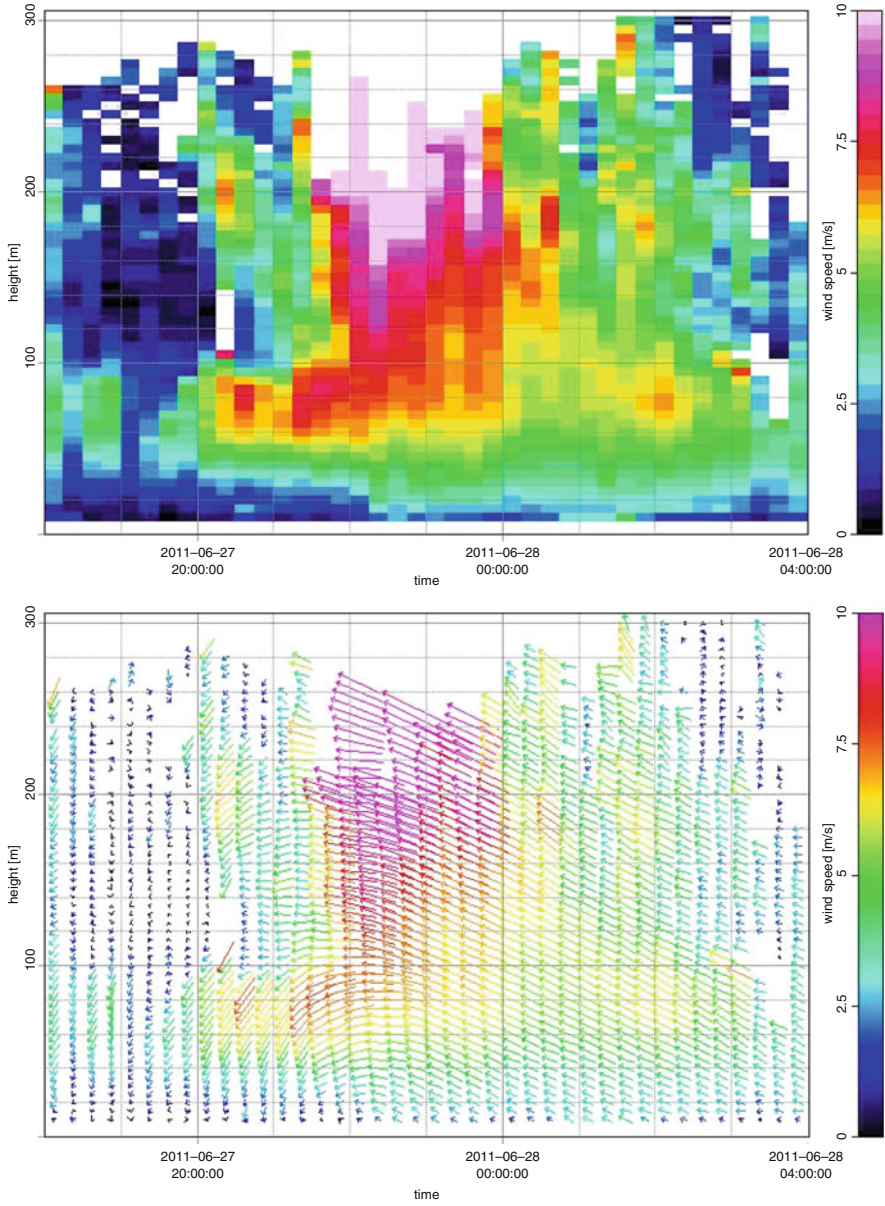
Fig. 11.9 Wind speed and wind vector measured with miniSODAR operated by the University of Georgia at the Köhlerloh Clearing for the period 18:00 June 26–04:00 June 27, with an LLJ on June 28 between 0:00 (height 180 m) and 2:30 (80 m)
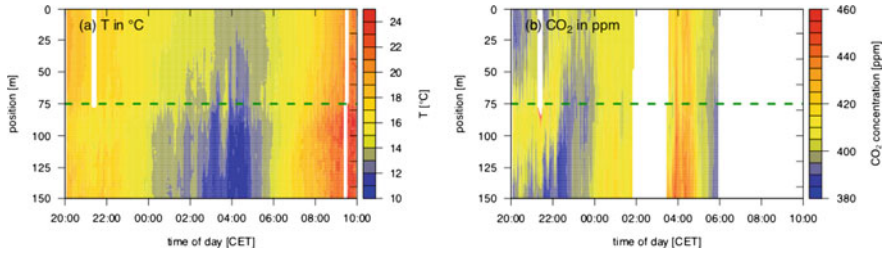
Fig. 11.10 Horizontal profiles measured with the HMMS from 27 June 20:00 CET to 28 June 2011 10:00 CET for temperature T (**a**) and CO_2 concentration (**b**). Position shows distance in meters, with starting point in the forest (0 m), forest edge (75 m), horizontal *green dotted line* and endpoint at the clearing (150 m). Remark: The color scaling is different in all graphs

mixed, and after 00:30 CET with the weakened LLJ event and lower wind velocities, there was an accumulation of CO_2 again over the total transect. Around 01:30 CET wind velocities up to $8\,\mathrm{ms}^{-1}$ led to an inflow of colder, CO_2-depleted air at the forest edge.

During 03:00–04:30 CET the wind direction changed in the height of 200–250 m to north, while above and below the wind direction was still south. The wind velocity was very low (less than $2\,\mathrm{ms}^{-1}$). The temperature decreased and the humidity increased during this situation. Unfortunately, CO_2 concentration measurements were not available up to that time due to connection failures. But at 03:30 CET there was another concentration minimum near the forest edge. After 04:00 CET the wind velocity increased to 4–$6\,\mathrm{ms}^{-1}$ at 100 m and the wind direction was again south. But because of the still weakened LLJ at this time, an accumulation of CO_2 could be observed. After 05:00 CET, the wind velocity increased at a height of 200 m to $10\,\mathrm{ms}^{-1}$ and the system was well mixed again.

11.3.2 Gravity Waves

Three main types of gravity waves are defined: high-frequency gravity waves, midrange gravity waves, and gravity waves with low frequencies. An overview of all types of gravity waves can be found in Nappo (2012). The work discussed here is related to gravity waves with low frequencies, so-called inertia-gravity waves.

The main characteristics of gravity waves are intrinsic frequency $\hat{\omega}$, zonal k, meridional l, and vertical m wavenumbers, phase $\hat{v}_p$ and group $\hat{c}_g$ velocities. Intrinsic frequency describes wave period in time domain $\hat{T}$ in the coordinate system moving with a wave, whereas horizontal and vertical wavenumbers represent horizontal (L_x, L_y) and vertical (L_z) wavelengths in spatial domain. Phase velocity is the speed at which a point of constant phase moves in the direction of the wave propagation. Gravity waves are dispersive waves. Therefore, the individual wave

components (and hence the energy) may move through the wave group with a group velocity as the group propagates along.

Almost all investigations of gravity waves have been done using the linear theory, which provides dependencies between wave characteristics under linearized solutions of fluid-dynamical equations. Following works of Cho (1995), Kunze (1985), and Sato (1994), the vertical shear effect in the background wind field was considered. To investigate inertia-gravity waves three relations were applied. The dispersion relation is given by

$$\hat{\omega}^2 = f_c^2 + \frac{N^2 k_h^2}{m^2} - \frac{2fk_h}{m}\frac{\partial \overline{v}}{\partial z}, \tag{11.8}$$

where f_c is the Coriolis parameter, N is the Brunt-Väisälä frequency, and $\partial \overline{v}/\partial z$ is the vertical wind shear component in direction perpendicular to gravity wave propagation, $k_h = \sqrt{k^2 + l^2}$ is horizontal wavenumber. The polarization relation is given by

$$R = \left| \frac{f_c}{\hat{\omega}} - \frac{k}{m\hat{\omega}}\frac{\partial \overline{v}}{\partial z} \right|, \tag{11.9}$$

where R is the axial ratio of the minor to the major axis of the polarization ellipse. The intrinsic frequency, i.e. the frequency in a coordinate system moving with the gravity wave, differs from the observed frequency which is relative to the fixed position at the ground. Therefore, the Doppler relation connects both frequencies:

$$\omega_{ob} = \hat{\omega} + \overline{u}k_h, \tag{11.10}$$

where ω_{ob} is the observed frequency and $\overline{u}$ is the mean background horizontal wind component in the same direction as the horizontal wavenumber k_h.

To examine background wind fields and localize wave motions in time and height, a wavelet transform has been applied to miniSODAR wind measurements. Figure 11.11 shows wavelet power spectra of zonal and meridional winds. The bold cyan line outlines the region with 95% significance level. The area above the green line (Fig. 11.11a, c) and on the right-hand side of the green line (Fig. 11.11b, d) indicates the cone of influence. The wavelet power spectra of time series (Fig. 11.11a, c) show significant wave periods between 0.6 and 1.1 h. The remarkable feature is that initially the wave motion is observed in the meridional wind between 20:00 and 22:00 CET on July 30 and then in the zonal wind between 22:00 and 24:00 CET on July 30. Furthermore, the significant vertical wavelength on the order of 30–70 m at the altitudes between 40 and 140 m was found in the wavelet power spectra of zonal and meridional wind profiles (Fig. 11.11b, d). In evaluating the results of the wavelet transform for the frequency content, bandpass filter parameters can be defined to filter out a gravity wave from the background wind fields. In this study the bandpass filter was constructed with a bandwidth of 0.6–1.6 h in the time and 20–90 m in the height. Fast Fourier transform (FFT) was
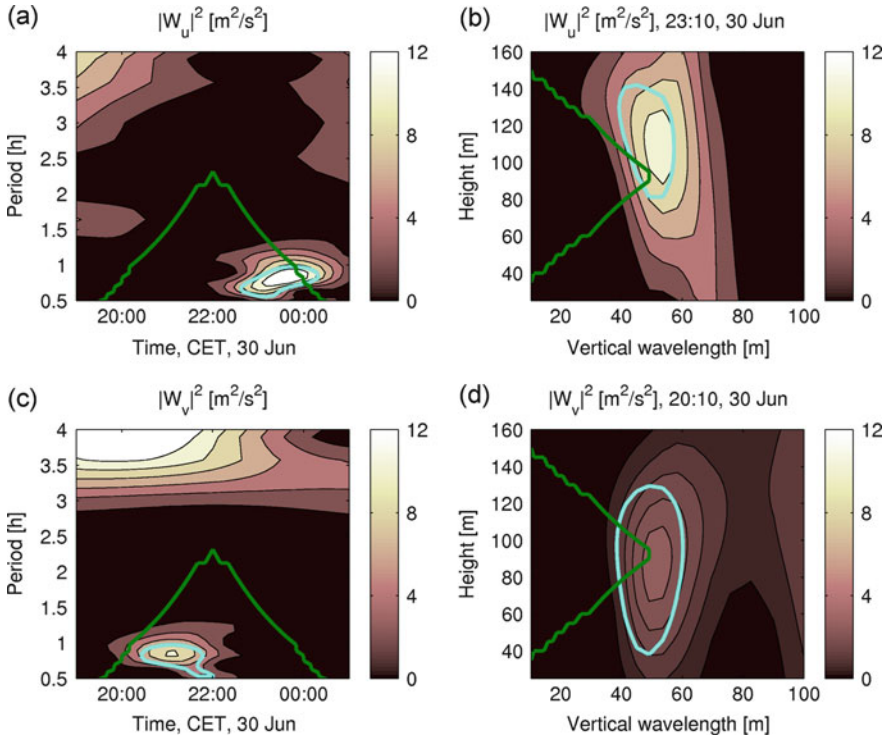
Fig. 11.11 Wavelet spectra of zonal (**a**, **b**) and meridional (**c**, **d**) winds. The *left panel* (**a**, **c**) shows wavelet spectra of the time series, the *right panel* (**b**, **d**) shows wavelet spectra of the height profiles

used to filter out the gravity wave with dominant observed frequency 64 min and wavelength 53 m. To avoid the sidelob effects and unwanted responses the signal was multiplied by the Hanning window. First, the FFT was applied to the time series and a mean contribution of each frequency was derived. By the removal of unwanted harmonics the range of interest (0.6–1.60 h) was selected and wind perturbations were obtained through a reconstruction using the inverse FFT and division by the Hanning window. The same principle was applied to vertical profiles of horizontal winds to derive wind perturbations in the range of interest of 20–90 m. The resulting wind perturbations are shown in Fig. 11.12. The dashed lines indicate lines of constant phase with preferred downward phase propagation. The vertical and temporal distances between the phase lines correspond to vertical wavelength and observed period detected with the wavelet transform (Fig. 11.11), respectively.
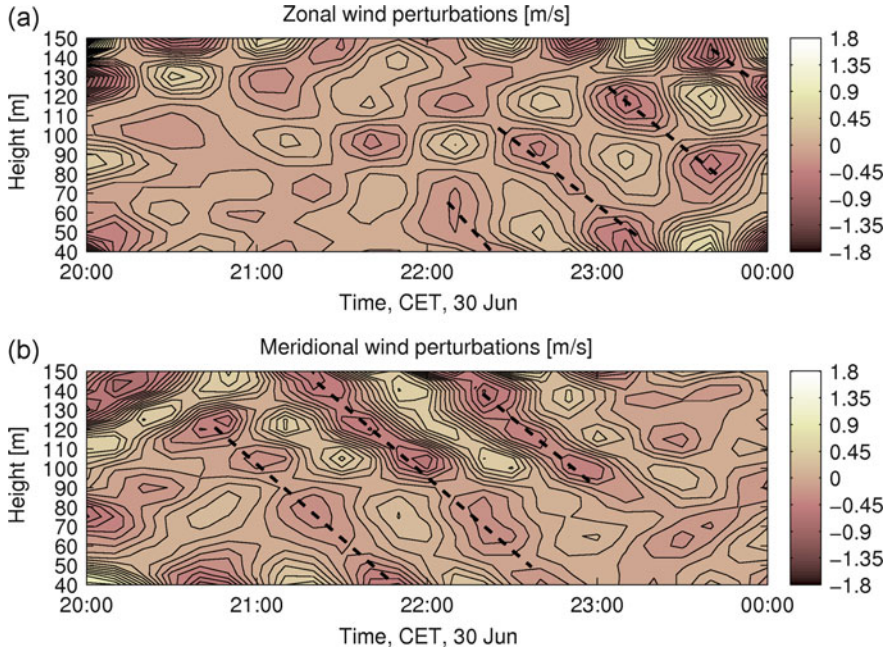
Fig. 11.12 Zonal (**a**) and meridional (**b**) wind perturbations on 30 June 2008 from 20:00 to 24:00 after band pass filtering with bandwidth of 0.6–16 h in time and 20–90 m in height

11.3.2.1 Rotary Spectrum

The rotary spectrum technique determines how energy is divided between upward and downward propagating gravity waves (Thompson 1978; Guest et al. 2000). The rotary spectrum is an asymmetric function represented by the fast Fourier transform of complex velocity vector profiles $u'(z) + iv'(z)$. The peaks in the spectrum indicate the presence of the gravity wave and the difference between amplitudes of the positive and negative parts of the spectrum allows the detection of the rotation direction of the horizontal wind perturbations with height. In the rotary spectrum, counterclockwise rotating waves are associated with positive frequencies, while clockwise rotating waves are associated with negative frequencies. It should be noted that in the northern hemisphere, counterclockwise rotation of horizontal wind perturbations with height indicates downward vertical energy propagation of a gravity wave, and clockwise rotation indicates upward vertical energy propagation of a gravity wave.

The analysis of the rotary spectrum reveals the presence of an inertia-gravity wave and its dominant vertical energy propagation. Figure 11.13 shows the rotary spectrum applied to wind perturbation after bandpass filtering with a bandwidth of 0.6–1.6 h in time and 20–90 m in height. The spectra were averaged for the period of wind rotation effect from 20:00 CET to 24:00 CET on June 30. The

Fig. 11.13 Rotary spectrum averaged for 4 h from 20:00 CET to 24:00 CET on 30 June 2008. Open circle, open diamond correspond to 95 and 99.9% significance levels, respectively
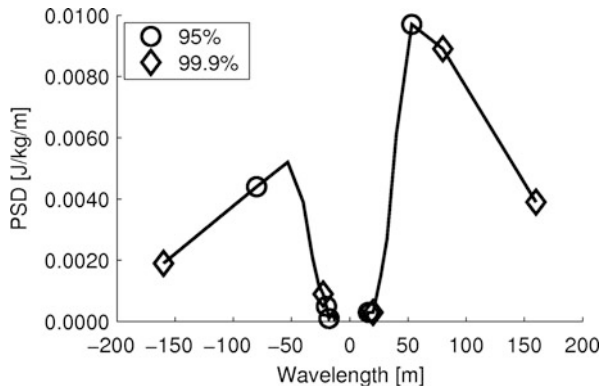
spectrum maximum indicates the presence of the gravity wave with the vertical period of 53 m. The rotary spectrum shows in its negative part the weaker clockwise rotational power corresponding to upward energy propagation and in its positive part the stronger counterclockwise rotational power corresponding to a dominant downward energy propagation, respectively. The spectrum is significant, except at the peak in the negative part due to the variability for the averaged period.
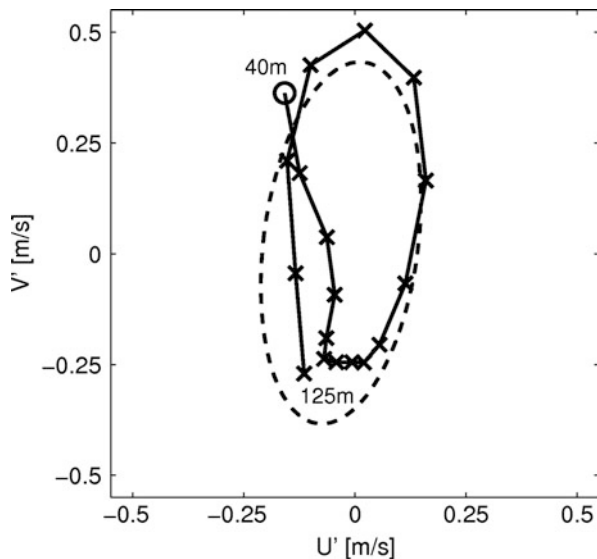
11.3.2.2 Hodograph Analysis

Hodograph analysis is used to estimate the intrinsic frequency of gravity wave $\hat{\omega}$, vertical wavelength L_z, and direction of the horizontal and vertical wave propagation. The hodograph is presented by a trace of the end of a wind perturbation vector with a height. If enough points are taken into account, then one vertical wavelength of gravity wave can be spawned, and an ellipse can be fitted.

Following linear theory without wind shear effect (Gill 1982), horizontal wind perturbations u' and v' depend on the intrinsic gravity wave $\hat{\omega}$ and Coriolis parameter f_c:

$$v' = -i \cdot u' \cdot \frac{f_c}{\hat{\omega}}. \tag{11.11}$$

Using Eq. (11.11) and the ratio of the minor and the major axis of the fitted ellipse, the intrinsic frequency $\hat{\omega}$ can be derived. The major axis of the hodograph is parallel to the direction of horizontal wave propagation undefined by 180°. A clockwise rotational sense of the hodograph in the northern hemisphere indicates upward energy propagation, whereas a counterclockwise rotational sense indicates downward energy propagation. The main disadvantage of the hodograph analysis is a high sensitivity to the applied filter used for the separation of a gravity wave from a mean flow (Zhang et al. 2004). This method is valid only for monochromatic waves and shows variable results in the case of the superposition of different waves.

Fig. 11.14 Hodograph of the wind perturbations measured at 22:30 CET on 30 June 2008 (solid line – measured profile, dashed line – fitted ellipse, open circle – starting point of the hodograph, labels correspond to height above the ground)

The hodograph analysis applied to the horizontal wind profile measured at 22:30 CET on June 30 (Fig. 11.14) reveals downward energy propagation from the counterclockwise rotational sense. The ratio of the fitted ellipse is 0.42 and the major axis is directed to 7° from the north. The full turn of the hodograph corresponds to the vertical wavelength on the order of 70 m, and the intrinsic period $2\pi/\hat{\omega}$ derived from the axes ratio of the fitted ellipse was found to be on the order of 6.6 h.

11.3.2.3   Stokes Parameter Spectra

To provide a more statistical description of the wave field, averaging over wavenumber band and over time duration of the gravity wave is required. These two factors are implemented in the Stokes parameter technique. The so-called Stokes parameters of gravity wave field I, D, P, Q were introduced by Vincent and Fritts (1987) and improved by Eckermann and Vincent (1989). This technique represents the vertical profile of horizontal wind perturbations as a partially polarized wave field. The four Stokes parameters I, D, P, Q then correspond to the total variance of gravity wave, axial anisotropy, "in-phase" covariance associated with linear polarization, and "in quadrature" covariance associated with circular wave polarization, respectively. The Stokes parameters can be defined in time or frequency spaces. In this work, Stokes parameters were derived in the frequency domain using fast

Fourier transform (Eckermann and Vincent 1989):

$$I_{m_1,m_2} = K \int_{m_1}^{m_2} \left(\overline{U_R^2(m)} + \overline{U_I^2(m)} + \overline{V_R^2(m)} + \overline{V_I^2(m)} \right) dm, \qquad (11.12)$$

$$D_{m_1,m_2} = K \int_{m_1}^{m_2} \left(\overline{U_R^2(m)} + \overline{U_I^2(m)} - \overline{V_R^2(m)} - \overline{V_I^2(m)} \right) dm, \qquad (11.13)$$

$$P_{m_1,m_2} = 2K \int_{m_1}^{m_2} \left(\overline{U_R(m)V_R(m)} + \overline{U_I(m)V_I(m)} \right) dm, \qquad (11.14)$$

$$Q_{m_1,m_2} = 2K \int_{m_1}^{m_2} \left(\overline{U_I(m)V_R(m)} + \overline{U_R(m)V_I(m)} \right) dm, \qquad (11.15)$$

where m is the vertical wavenumber, U_R, V_R are the real parts of the spectra and U_I, V_I are the imaginary parts of the spectra of wind perturbation profiles $u'(z)$ and $v'(z)$, overbars denote averages over a number of independent spectral realizations to remove the effects of incoherent motions, and K is a constant which scales the squared Fourier terms to power spectral densities. Using the derived Stokes parameters, the degree of the gravity wave polarization d_{m_1,m_2}, phase difference δ_{m_1,m_2} between zonal and meridional wind perturbations, the major axis orientation Θ_{m_1,m_2}, and the averaged ellipse axial ratio R_{m_1,m_2} are estimated:

$$d_{m_1,m_2} = \frac{(D_{m_1,m_2}^2 + P_{m_1,m_2}^2 + Q_{m_1,m_2}^2)^{\frac{1}{2}}}{I_{m_1,m_2}} \qquad (11.16)$$

$$\delta_{m_1,m_2} = \arctan\left(\frac{Q_{m_1,m_2}}{P_{m_1,m_2}} \right) \qquad (11.17)$$

$$\Theta_{m_1,m_2} = \frac{1}{2} \arctan\left(\frac{P_{m_1,m_2}}{D_{m_1,m_2}} \right) \qquad (11.18)$$

$$R_{m_1,m_2} = \tan \alpha \qquad (11.19)$$

where

$$\alpha = \frac{1}{2} \arcsin\left(\frac{Q_{m_1,m_2}}{d_{m_1,m_2} \cdot I_{m_1,m_2}} \right) \qquad (11.20)$$

The most attractive feature of this analysis is that the wave motion is well described due to the averaging in time and wave number bands, which can be selected on the basis of the times and wavelengths of the maxima located in the wavelet spectra.

To achieve a more statistical description of the gravity wave field, the Stokes parameter technique was applied. The Stokes parameters derived from miniSODAR measurements and averaged over the period 20:00–24:00 June 30 are presented in Table 11.1. The ratio of the polarization ellipse was found to be on the order of 0.65 and the major axis is directed to 31.2° from the north.

Table 11.1 Stokes parameters derived from miniSODAR measurements on 30 June 2008

Filter band (time, height)	0.6–1.6 h, 20–90 m
Averaged time (CET)	20:00–24:00 30 June, 2008
Degree of polarization, d_{m_1,m_2}	0.28
Major axis orientation, Θ_{m_1,m_2}	31.2°
Phase difference, δ_{m_1,m_2}	−68.8°
Ellipse axial ratio,	0.65

**Table 11.2** Gravity wave parameters derived from analysis of Stokes parameter spectra

Mean horizontal wind, $\overline{U}$, ms^{-1} (in the wave propagation direction)	−1.8
Wind shear component, $\partial \overline{V}/\partial z$, s^{-1}	$2.9 \cdot 10^{-3}$
Brunt-Väisälä frequency, N, s^{-1}	$11.9 \cdot 10^{-3}$
Coriolis parameter, f, rad s^{-1}	$11.2 \cdot 10^{-5}$
Intrinsic period, $2\pi/\hat{\omega}$, h	7.3
Observed period, $2\pi/\omega_{ob}$, h	1.06
Horizontal wavelength, $2\pi/k_h$, km	−3.4
Vertical wavelength, $2\pi/m$, m	53.3
Horizontal phase velocity, $\hat{v}_{ph}$, ms^{-1}	$-13.0 \cdot 10^{-2}$
Vertical phase velocity, $\hat{v}_{pz}$, ms^{-1}	$0.2 \cdot 10^{-2}$
Horizontal group velocity, $\hat{c}_{gh}$, ms^{-1}	$-9.0 \cdot 10^{-2}$
Vertical group velocity, $\hat{c}_{gz}$, ms^{-1}	$-0.14 \cdot 10^{-2}$

11.3.2.4   Gravity Wave Characteristics

To derive the gravity wave characteristics, a solution of three equations was used: the dispersion relation (Eq. (11.8)), the polarization relation (Eq. (11.9)), and the Doppler equation (Eq. (11.10)). The ellipse ratio R_{m_1,m_2} was obtained by the Stokes parameter analysis, and the vertical wavenumber m is given by the evaluation of the wavelet or fast Fourier transforms (Figs. 11.11b, d and 11.13). The coordinate system was rotated to the direction of the wave propagation Θ_{m_1,m_2} obtained by the Stokes parameter technique. In this system the mean horizontal wind component U is oriented in the wave propagation direction and the mean horizontal wind component V is oriented perpendicular to the direction of the wave propagation Θ_{m_1,m_2}. The Brunt-Väisälä frequency N was derived from temperature measurements with the SODAR/RASS system and the Coriolis parameter f is a constant for a given location (the value over the Waldstein site is $11.2 \cdot 10^{-5}$ rad s^{-1}). Then Eqs. (11.8) and (11.9) were then solved to obtain the intrinsic frequency $\hat{\omega}$ and the horizontal wavenumber k. The derived gravity wave characteristics are presented in Table 11.2.

The results indicate that a gravity wave with horizontal wavelength on the order of 3.4 km, intrinsic period 7.6 h, and vertical wavelength ∼53 m occurred over the measuring site. Due to the Doppler effect the observed period of the wave relative to the fixed position was found to be on the order of 1.06 h. As was mentioned above the wave propagation direction obtained with hodograph analysis and Stokes
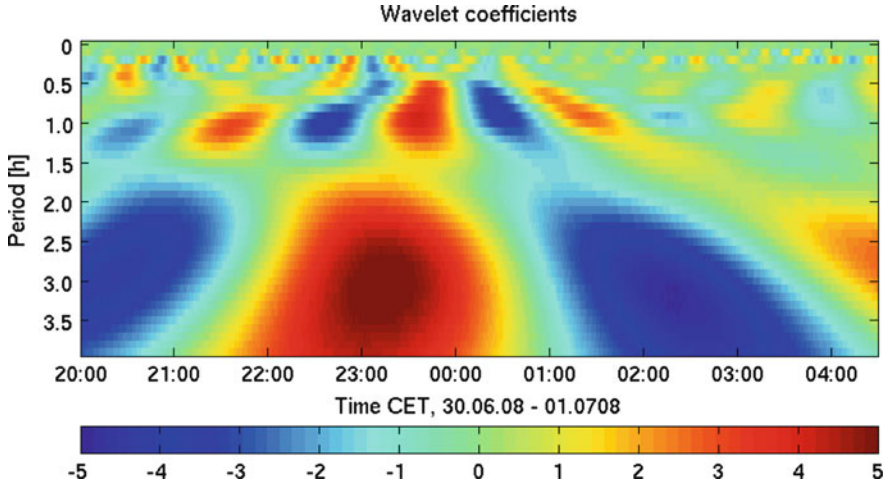
Fig. 11.15 Wavelet coefficients derived from the vertical wind measurements at 36 m height for the period June 30–July 01, 2008 during IOP 2

parameter spectra is undefined by 180°. It should be noted that the Doppler relation between intrinsic and observed periods of the detected gravity wave (Eq. (11.10)) is sensitive to the background wind speed, but the equation is fulfilled only if the propagation from south-west to north-east is selected, resulting in the negative horizontal wavenumber.

These results were confirmed by wind measurements with an ultrasonic anemometer installed at the top of TT. To detect wave frequencies over the canopy during the wind rotation event, 2 Hz wind measurements for the period 20:00 June 30–04:00 July 01, 2008 have been used. Fig. 11.15 shows the coefficients of the wavelet transform derived using Eq. (11.6). Besides the vertical wind oscillation with a period of 3.2 h lasting through the entire time, one can see the wave event with a period ∼1 h which arises shortly after 20:00 and vanishes around 02:00.

Using the method described in Chap. 6, coherent structures were extracted from turbulent time series, and Reynolds fluxes and fluxes transported by these structures were estimated. Figure 11.16 shows the number of coherent structures detected and their frequencies for the period of 4 h before the detected gravity wave event (crosses) and during the gravity wave appearance (circles). Each point indicates a mean duration of coherent structures for a 30 min interval detected as a peak in the wavelet variance spectrum. The dashed and solid lines represent the linear regression model fitted for both periods, respectively. As shown in Fig. 11.16, the number of detected coherent structures slightly increases and higher frequencies or short structures are observed during the gravity wave occurrence in contrast to the preceding period.

A clear impact of gravity wave propagation over a measuring site was found in the turbulent momentum exchange. As shown in Fig. 11.17 (black line) the
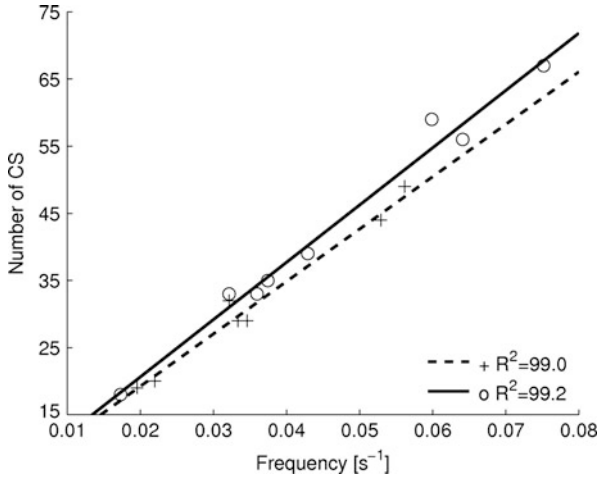
Fig. 11.16 Number of coherent structures and their frequencies detected for the period 16:00–20:00 (*crosses*) and 20:00–24:00 (*circles*) June 30, 2008. *Dashed and solid lines* represent the linear regression model for both periods, respectively
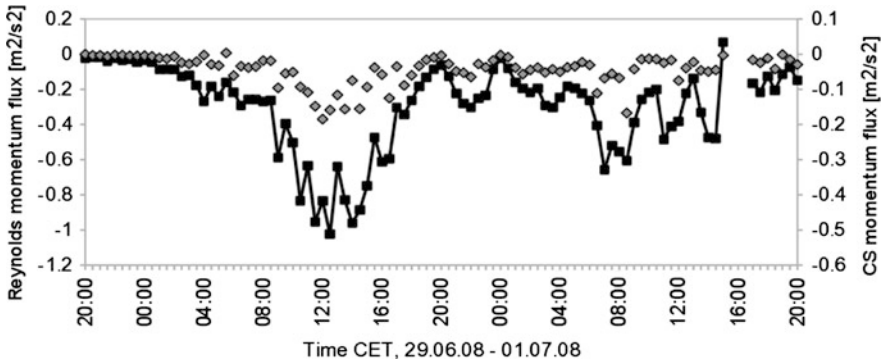

Fig. 11.17 Reynolds momentum flux (black line), momentum flux transported by coherent structures (gray dots) measured at the height 36 m for the period June 29–July 01, 2008 during IOP 2

estimated Reynolds-averaged momentum flux reaches the first maximum on the order of 1.1 $m^2 s^{-2}$ around noon and the second maximum is observed between 20:00 and 24:00 when the gravity wave occurs. During this period the momentum transport by coherent structures is higher as well (Fig. 11.17 grey points) and reaches 20% of the Reynolds flux. The sensible heat, latent heat and carbon dioxide fluxes are not affected by the gravity wave (not shown here).

Partitioning the momentum flux transported by coherent structures during ejection and sweep phases (Fig. 11.18 black line and grey points, respectively), one can see that before the gravity wave appears momentum above the canopy is transported

Fig. 11.18 Ratio of the flux transported during the ejection phase to the total flux transported by coherent structures (*black line*) and ratio of the flux transported during the sweep phase to the total momentum flux transported by coherent structures (*gray line*) for the momentum coherent exchange measured at the height 36 m for the period June 29–July 01, 2008 during IOP 2
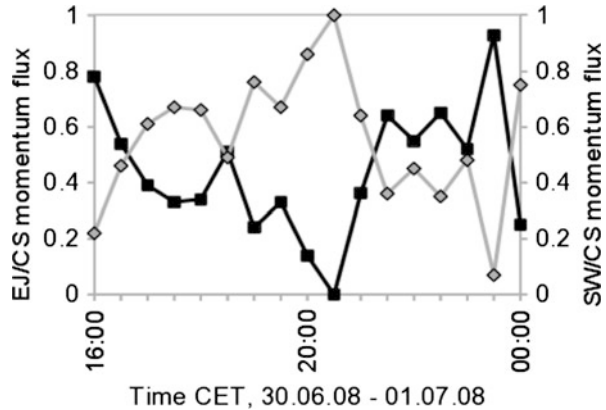
mostly by "sweeps" events reaching almost 100% at 20:00, whereas after that the contribution of the "ejection" phases is higher to the momentum transport. This suggests that turbulent exchange by sweep motions is suppressed by downward propagated gravity waves, whereas the ejections are compensating for this effect.

11.4   Conclusions

Nocturnal carbon dioxide fluxes measured using eddy-covariance technique are influenced by non-stationary atmospheric processes. The boundary-layer phenomena such as low-level jets are able to generate wind shear and turbulence close to the surface. Low-level jets influence transport processes at the spatial scale of the measuring site and may re-distribute vertical concentration profiles and increase surface fluxes due to strong vertical shear. Changes of CO_2 concentration perpendicular to the forest edge indicate that the contribution of coherent structures and their scale plays an important role in transport processes in heterogeneous areas. These phenomena have to be taken into account when analyzing long term carbon flux measurements, especially for the sites located over flat terrain, because they are highly susceptible to the occurrence of low-level jets. The increased shear caused by low-level jets also leads to a better mixing of trace gases such as NO and O_3 at the forest floor and in the canopy.

Moreover, wind shear is one of the main sources of gravity waves. A complete study of the gravity wave characteristics and wave effects on the coherent momentum exchange above the canopy level has been presented. The gravity wave, detected during the second intensive observation period IOP 2 of the EGER project, was connected to the wind rotation and wind shear event in the ascending LLJ observed in the Fichtelgebirge mountains, North-Eastern Bavaria, Germany.

To filter out the wind perturbations associated with the gravity wave, the wavelet transform of the mean wind measurements was used. The wave characteristics were analyzed using the rotary spectrum, hodograph, and Stokes-parameter spectral analysis. Evaluation of the equations of the linear theory showed that the wave propagates from south-west to north-east and has the intrinsic period 7.3 h, which due to the Doppler shift corresponds to the observed period of about 64 min. The derived horizontal and vertical wavelengths were on the order of -3.4 km and 53 m, respectively. During the wave event the analysis revealed stronger counterclockwise rotational power corresponding to the downward energy at the height range of 40–120 m.

The impact of the downward wave energy propagation on the turbulent momentum exchange above the forest measuring site was found. It was shown that coherent structures have smaller time scales when the gravity wave is observed. Finally, the occurrence of a gravity wave in the vicinity of the canopy leads to a higher transport of the momentum and an increase of the turbulent exchange by coherent structures. The partitioning of the momentum transport between the sweep and ejection phases of coherent structures shows a higher activity of sweeps in the turbulent momentum exchange before the gravity wave event and higher momentum transport by the ejection phases when the gravity wave is observed.

This study has shown that the ecosystem fluxes are affected by different atmospheric phenomena occurring up to several hundred meters above the ground, and such processes as wind shear, low-level jets, and gravity waves should not be neglected in the analysis of turbulent fluxes, and the effects of these have to be investigated along with other surface processes.

References

Antonia RA (1981) Conditional sampling in turbulence measurements. Ann Rev Fluid Mech 13:131–156. doi:10.1146/annurev.fl.13.010181.001023

Baas AFD, Driedonks AGM (1985) Internal gravity waves in a stably stratified boundary layer. Bound-Layer Meteorol 31:303–323

Baldocchi D, Falge E, Lianhong G, Olson R, Hollinger D, Running S, Anthoni P, Bernhofer C, Davis K, Evans R, Fuentes J, Goldstein A, Katul G, Law B, Lee X, Malhi Y, Meyers T, Munger W, Oechel W, Paw U KT, Pilegaard K, Schmid HP, Valentini R, Verma S, Vesala T, Wilson K, Wofsy S (2001) FLUXNET: a new tool to study the temporal and spatial variability of ecosystem-scale carbon dioxide, water vapor, and energy flux densities. Bull Am Meteorol Soc 82:2415–2434

Banta RM, Newsom RK, Lundquist JK, Pichugina YL, Coulter RL, Mahrt L (2002) Nocturnal low-level jet characteristics over Kansas during cases-99. Bound-Layer Meteorol 105:221–252

Bergström H, Högström U (1989) Turbulent exchange above a pine forest II. Organized structures. Bound-Layer Meteorol 49:231–263. doi:10.1007/BF00120972

Blackadar AK (1957) Boundary layer wind maxima and their significance for the growth of nocturnal inversions. Bull Am Meteorol Soc 38:283–290

Bonner WD (1968) Climatology of the low level jet. Mon Weather Rev 96:833–850

Brunet Y, Collineau S (1994) Wavelet analysis of diurnal and nocturnal turbulence above a maize canopy. In: Foufoula-Georgiou E, Kumar P (eds) Wavelets in geophysics, wavelet analysis and its applications, vol 4. Academic Press, San Diego, pp 129–150

Brunet Y, Irvine MR (2000) The control of coherent eddies in vegetation canopies: streamwise structure spacing, canopy shear scale and atmospheric stability. Bound-Layer Meteorol 94:139–163. doi:10.1023/A:1002406616227

Cava D, Giostra U, Siqueira M, Katul G (2004) Organised motion and radiative perturbations in the nocturnal canopy sublayer above an even-aged pine forest. Bound-Layer Meteorol 112:129–157. doi:10.1023/B:BOUN.0000020160.28184.a0

Chen J, Hu F (2003) Coherent structures detected in atmospheric boundary-layer turbulence using wavelet transforms at Huaihe River Basin, China. Bound.-Layer Meteorol 107:429–444. doi:10.1023/A:1022162030155

Cheng Y, Parlange MB, Brutsaert W (2005) Pathology of Monin-Obukhov similarity in the stable boundary layer. J Geophys Res 110:D06,101. doi:10.1029/2004JD004923

Cho J (1995) Inertio-gravity wave parameter estimation from cross-spectral analysis. J Geophys Res 100:18,727–18,737

Clifford SF, Kaimal JC, Lataitis RJ, Strauch RG (1994) Ground-based remote profiling in atmospheric studies - an overview. In: Proceedings of the IEEE, vol 82, pp 313–355

Eckermann S, Vincent R (1989) Falling sphere observations gravity waves motions in the upper stratosphere over Australia. Pageoph 130:509–532

Einaudi F, Finnigan JJ (1993) Wave-turbulence dynamics in the stably stratified boundary layer. J Atmos Sci 50:1841–1864. doi:10.1175/1520–0469(1993)050<1841:WTDITS>2.0.CO;2

Finnigan J (2000) Turbulence in plant canopies. Ann Rev Fluid Mech 32:519–571. doi:10.1146/annurev.fluid.32.1.519

Foken T, Meixner F, Falge E, Zetzsch C, Serafimovich A, Bargsten A, Behrendt T, Biermann T, Breuninger C, Dix S, Gerken T, Hunner M, Lehmann-Pape L, Hens K, Jocher G, Kesselmeier J, Lüers J, Mayer JC, Moravek A, Plake D, Riederer M, Rütz F, Scheibe M, Siebicke L, Sörgel M, Staudt K, Trebs I, Tsokankunku A, Welling M, Wolff V, Zhu Z (2012) Coupling and exchange of energy and reactive and non-reactive trace gases at a forest site results of the EGER experiment. Atmos Chem Phys 12:1923–1950. doi:10.5194/acp-12-1923-2012

Foster RC, Vianey F, Drobinski P, Carlotti P (2006) Near-surface coherent structures and the vertical momentum flux in a large-eddy simulation of the neutrally-stratified boundary layer. Bound-Layer Meteorol 120:229–255. doi:10.1007/s10546-006-9054-8

Gao W, Shaw RH, Paw U KT (1989) Observation of organized structure in turbulent flow within and above a forest canopy. Bound-Layer Meteorol 47:349–377. doi:10.1007/BF00122339

Gerstberger P, Foken T, Kalbitz K (2004) The Lehstenbach and Steinkreuz chatchments in NE Bavaria, Germany. In: Matzner E (ed) Biogeochemistry of forested catchments in a changing environment: ecological Studies, vol 172. Springer, Heidelberg, pp 15–41

Gill AE (1982) Atmosphere-Ocean dynamics. Academic, San Diego

Gossard EE, Hooke WH (1975) Waves in the atmosphere. Elsevier, New York

Grossmann A, Morlet J (1984) Decomposition of hardy functions into square integrable wavelets of constant shape. J Math Anal 15:723–736

Guest FM, Reeder MJ, Marks CJ, Karoly DJ (2000) Inertia-gravity waves observed in the lower stratosphere over Macquarie Island. J Atmos Sci 57:737–752

Hoffmann P, Rapp M, Serafimovich A, Latteck R (2005) On the occurrence and formation of multiple layers of polar mesosphere summer echoes. Geophys Res Lett 32, L05812. doi:10.1029/2004GL021409

Holton J (1967) The diurnal boundary layer wind oscillation above sloping terrain. Tellus 19:199–205

Hübner J, Olesch J, Falke H, Meixner FX, Foken T (2014) A horizontal mobile measuring system for atmospheric quantities. Atmos Meas Tech 7:2967–2980

Karipot A, Leclerc MY, Zhang G, Martin T, Starr G, Hollinger D, McCaughey JH, Hendrey GR (2006) Nocturnal CO_2 exchange over a tall forest canopy associated with intermittent low-level jet activity. Theor Appl Climatol 85:243–248

Katul G, Kuhn G, Schieldge J, Hsieh CI (1997) The ejection-sweep character of scalar fluxes in the unstable surface layer. Bound-Layer Meteorol 83:1–26. doi:10.1023/A:1000293516830

King JC, Mobbs SD, Darby MS, Rees JM (1987) Observations of an internal gravity wave in the lower troposphere at Halley, Antarctica. Bound-Layer Meteorol 39:1–13. doi:10.1007/BF00121862

Koch SE, O'Handley C (1997) Operational forecasting and detection of mesoscale gravity waves. Wea Forecast 12:253–281. doi:10.1175/1520-0434(1997)012<0253:OFADOM>2.0.CO;2

Kronland-Martinet R, Morlet J, Grossmann A (1987) Analysis of sound patterns through wavelet transforms. Int J Pattern Recognit Artif Intell 1:273–302

Kumar P, Foufoula-Georgiou E (1997) Wavelet analysis for geophysical applications. Rev Geophys 35:385–412

Kunze E (1985) Near-inertial wave propagation in geostrophic shear. J Phys Oceanogr 15:544–565

Lee X, Neumann H, Hartog G, Mickle R, Fuentes J, Black T, Yang P, Blanken P (1997) Observation of gravity waves in a boreal forest. Bound-Layer Meteorol 84:383–398. doi:10.1023/A:1000454030493

Lehmann V, Dibbern J, Görsdorf U, Neuschaefer J, Steinhagen H (2003) The new operational UHF wind profiler radars of the deutscher wetterdienst. In: Wandinger U, Engelmann R, Schmieder K (eds) 6th International Symposium on Tropospheric Proling (ISTP) - extended abstracts. Institute for Tropospheric Research, pp 489–491

Lindzen RS, Tung KK (1976) Banded convective activity and ducted gravity waves. Mon Weather Rev 104:1602–1617. doi:10.1175/1520-0493(1976)1048<1602:BCAADG>2.0.CO;2

Maitani T, Shaw RH (1990) Joint probability analysis of momentum and heat fluxes at a deciduous forest. Bound-Layer Meteorol 52:283–300. doi:10.1007/BF00122091

Nappo CJ (2012) An introduction to atmospheric gravity waves. International geophysics series, vol 102. Academic, San Diego

Nappo CJ, Miller DR, Hiscox AL (2008) Wave-modified flux and plume dispersion in the stable boundary layer. Bound-Layer Meteorol 129:211–223. doi:10.1007/s10546-008-9315-9

Paw U KT, Brunet Y, Collineau S, Shaw RH, Maitani T, Qiu J, Hipps L (1992) On coherent structures in turbulence above and within agricultural plant canopies. Agric For Meteorol 61:55–68

Pecnick MJ, Young JA (1984) Mechanics of a strong subsynoptic gravity wave deduced from satellite and surface observations. J Atmos Sci 41:1850–1862. doi:10.1175/1520-0469(1984)041<1850:MOASSG>2.0.CO;2

Pike CJ (1994) Analysis of high resolution marine seismic data using wavelet transform. In: Foufoula-Georgiou E, Kumar P (eds) Wavelets in geophysics. Wavelet analysis and its applications, vol 4. Academic, San Diego, pp 183–211

Raupach MR, Thom AS (1981) Turbulence in and above plant canopies. Ann Rev Fluid Mech 13:97–129

Raupach MR, Finnigan JJ, Brunet Y (1996) Coherent eddies and turbulence in vegetation canopies: the mixing-layer analogy. Bound-Layer Meteorol 78:351–382. doi:10.1007/BF00120941

Rees JM, Staszewskib WJ, Winklerc JR (2001) Case study of a wave event in the stable atmospheric boundary layer overlying an Antarctic Ice Shelf using the orthogonal wavelet transform. Dyn Atmos Oceans 34:245–261. doi:10.1016/S0377-0265(01)00070-7

Sato K (1994) A statistical study of the structure, saturation and sources of inertia-gravity waves in the lower stratosphere observed with the MU radar. J Atmos Terr Phys 56:755–774

Sauvageot H (1992) Radar meteorology. Artech House, Boston

Serafimovich A, Thomas C, Foken T (2011) Vertical and horizontal transport of energy and matter by coherent motions in a tall spruce canopy. Bound-Layer Meteorol 140:429–451. doi:10.1007/s10546-011-9619-z

Shaw RH, Paw U KT, Gao W (1989) Detection of temperature ramps and flow structures at a deciduous forest site. Agric For Meteorol 47:123–138

Smedman AS, Bergström H, Högström U (1995) Spectra, variances and length scales in a marine stable boundary layer dominated by a low level jet. Bound-Layer Meteorol 76:211–232. doi:10.1007/BF00709352

Staudt K, Foken T (2007) Documentation of reference data for the experimental areas of the Bayreuth Centre for Ecology and Environmental Research (BayCEER) at the Waldstein site. Arbeitsergebnisse, Universität Bayreuth, Abt Mikrometeorologie. Print, ISSN:1614-8916 35:37

Stull RB (1988) An introduction to boundary layer meteorology. Kluwer Academic Publishers, Dordrecht/Boston/London

Sun J, Lenschow DH, Burns SP, Banta RM, Newsom RK, Coulter R, Frasier S, Ince T, Nappo C, Balsley BB, Jensen M, Mahrt L, Miller D, Skelly B (2003) Atmospheric disturbances that generate intermittent turbulence in nocturnal boundary layers. Bound-Layer Meteorol 110:255–279. doi:10.1023/A:1026097926169

Thomas C, Foken T (2005) Detection of long-term coherent exchange over spruce forest using wavelet analysis. Theor Appl Climatol 80:91–104. doi:10.1007/s00704-004-0093-0

Thomas C, Foken T (2007a) Flux contribution of coherent structures and its implications for the exchange of energy and matter in a tall spruce canopy. Bound-Layer Meteorol 123:317–337. doi:10.1007/s10546-006-9144-7

Thomas C, Foken T (2007b) Organised motion in a tall spruce canopy: temporal scales, structure spacing and terrain effects. Bound-Layer Meteorol 122:123–147. doi:10.1007/s10546-006-9087-z

Thomas C, Mayer JC, Meixner FX, Foken T (2006) Analysis of low-frequency turbulence above tall vegetation using a doppler sodar. Bound-Layer Meteorol 119:563–587

Thompson R (1978) Observation of inertial waves in the stratosphere. Q J R Meteorol Soc 104:691–698

Torrence C, Compo GP (1998) A practical guide to wavelet analysis. Bull Am Meteorol Soc 79(1):61–78

Vickers D, Mahrt L (1997) Quality control and flux sampling problems for tower and aircraft data. J Atmos Ocean Tech 14:512–526. doi:10.1175/1520-0426(1997)014<0512:QCAFSP>2.0.CO;2

Vincent R, Fritts D (1987) A climatology of gravity wave motions in the mesopause region at Adelaide, Australia. J Atmos Sci 44:748–760

Wilczak JM, Oncley SP, Stage SA (2001) Sonic anemometer tilt correction algorithms. Bound-Layer Meteorol 99:127–150. doi:10.1023/A:1018966204465

Zhang F, Wang S, Plougonven R (2004) Uncertainties in using the hodograph method to retrieve gravity wave characteristics from individual soundings. Geophys Res Lett 31:L11110. doi:10.1029/2004GL019841

Zink F, Vincent R (2001) Wavelet analysis of stratospheric gravity wave packets over Macquarie Island. J Geophys Res 106:10275–10288

Zülicke C, Peters D (2006) Simulation of inertiagravity waves in a poleward-breaking Rossby wave. J Atmos Sci. doi:10.1175/JAS3805.1